

**High-efficiency, anode-free lithium-metal batteries with a close-packed homogeneous lithium morphology**

Journal:	<i>Energy & Environmental Science</i>
Manuscript ID	EE-ART-10-2021-003103.R1
Article Type:	Paper
Date Submitted by the Author:	15-Dec-2021
Complete List of Authors:	Su, Laisuo; The University of Texas at Austin Charalambous, Harry; Argonne National Laboratory Advanced Photon Source Cui, Zehao; The University of Texas at Austin, Materials Science and Engineering Manthiram, Arumugam; The University of Texas at Austin, Materials Science and Engineering

ARTICLE

High-efficiency, anode-free lithium-metal batteries with a close-packed homogeneous lithium morphology

Laisuo Su,^a Harry Charalambous,^b Zehao Cui^a and Arumugam Manthiram*^aReceived 00th January 20xx,
Accepted 00th January 20xx

DOI: 10.1039/x0xx00000x

Anode-free lithium-metal batteries (LMBs) are ideal candidates for high-capacity energy storage as they eliminate the need of a conventional graphite electrode or excess lithium-metal anode. Current anode-free LMBs suffer from low Coulombic efficiency (CE) due to poor lithium stripping efficiency. Advanced electrolyte development is a promising route to maximize lithium plating and stripping CE and minimize capacity fade. However, a poor understanding of the mechanisms by which advanced electrolytes improve performance hampers progress in the practical development of anode-free LMBs. Here, we use synchrotron techniques and other tools to analyze the influence of three commercially available electrolytes on the composition, heterogeneity, kinetics, morphology, and electrochemistry of anode-free LMBs. Advanced electrolytes improve the electrochemical performance of anode-free LMBs by forming much denser and better-packed Li morphologies on Cu current collector than the conventional electrolyte. Li plates uniformly over the electrode area with the advanced electrolytes rather than in a few active sites. Inactive crystalline Li with heterogeneous distribution dominates the capacity degradation of anode-free cells, especially with the conventional electrolyte, indicating that reducing the amount of “dead” crystalline Li will significantly improve the cycling stability of anode-free cells. The understanding of Li plating and stripping process obtained from this work will accelerate the development of anode-free LMBs with high efficiency.

Broader context

Lithium-ion battery (LIB) packs have achieved long cycle life (> 1,000 cycles), fast (dis)charge rates (> 1C), high energy density (> 150 Wh kg⁻¹, 250 Wh L⁻¹), and low cost (< 300 US\$ kWh⁻¹). However, LIBs with graphite anode can hardly reach the US Department of Energy's goals of 235 Wh kg⁻¹, 500 Wh L⁻¹, and 125 US\$ kWh⁻¹ for electric vehicles, necessitating alternative anode platforms. Anode-free lithium-metal batteries (LMBs) are a promising candidate because they can deliver 40-60% more energy density by removing the graphite anode. The adoption of LMBs is limited by poor cycling stability and safety due to the uncontrollable growth of Li on the anode with traditional electrolytes. Advanced electrolytes have recently been developed to improve the cycling stability of LMBs. Understanding the mechanisms of the improved performance is imperative for the development of next-generation electrolytes to enable a wide application in electric vehicles. As a non-destructive tool, synchrotron X-ray diffraction can probe a real cell and provide spatial and temporal information of its crystalline components. The distribution and the evolution of crystalline Li on the anode was monitored in cells with different electrolytes. The methodology can be combined with insights from laboratory characterization techniques to aid the development of electrolytes that can control the growth of Li on the anode and enable the adoption of anode-free LMBs with long cycle life.

Introduction

The development of lithium-ion batteries (LIBs) has enabled the rapid growth of electric vehicle market.¹⁻² High energy-density LIBs can increase the range of electric vehicles as well as reduce the cost. Lithium-metal batteries (LMBs) can further increase the specific energy by 35% and energy density by 50% at the cell level by eliminating the conventional graphite anode electrodes.³ Moreover, anode-free LMBs deliver 60% higher energy density compared to traditional LIBs by using a bare Cu foil with no anode-active material.⁴ However, the adoption of LMBs and anode-free LMBs is limited due to their rapid capacity

fade and safety concerns.⁵ Researchers are attacking this problem from multiple directions, from tailoring the anode morphology⁶ to engineering the solid electrolyte interphase⁷ to developing advanced electrolytes.⁴

Recent studies have demonstrated that the choice of electrolyte significantly affects the performance of anode-free LMBs.^{4,8} As metallic Li is thermodynamically unstable with almost all organic solvents and lithium salts,⁹ forming a homogeneous and stable solid-electrolyte-interphase (SEI) on the surface of the anode is crucial to achieving high cycling stability and safety of LMBs.¹⁰ Li nucleation and growth kinetics on the anode are influenced by the electrolyte, and thus developing advanced electrolytes is critical for high-performance of anode-free LMBs. For example, Ren *et al.* developed a localized high-concentration electrolyte (LHCE) that extends anode-free cells to 70 cycles with 80% capacity retention under practical conditions.¹¹ Bao's group developed a single-solvent, single-salt electrolyte, which enables 80% capacity retention of anode-free cells after 100 cycles.⁸ Dahn's

^a Materials Science and Engineering Program & Texas Materials Institute, The University of Texas at Austin, Austin, TX 78712, United States. E-mail: manth@austin.utexas.edu

^b Advanced Photon Source, Argonne National Laboratory, 9700 S. Cass Avenue, Lemont, IL 60439, United States.

† Electronic Supplementary Information (ESI) available. See DOI: 10.1039/x0xx00000x

group developed a high-concentration dual-salt carbonate electrolyte that extends the lifetime of anode-free cells to 200 cycles under certain experimental conditions (high pressure, small C-rates).⁴

Understanding the mechanisms by which advanced electrolytes improve the cycling stability is crucial for designing stable LMBs and anode-free LMBs. Postmortem techniques have been widely applied to study the effect of salts and solvents on the performance of LMBs. By applying *ex-situ* X-ray photoelectron spectroscopy (XPS) and transmission electron microscopy (TEM), Jung *et al.* discovered that the Li plating morphology rather than the chemical composition of the SEI contributes to better cycling performance.¹² Wang *et al.* utilized the *ex-situ* cryo-TEM technique to study the evolving nanostructure of Li metal, in which glassy Li and crystalline Li transition was observed at different current densities and deposition time.¹³ They suggested that advanced electrolytes promote the formation of glassy Li, leading to better cycling stability. Fang *et al.* developed a gas titration chromatography to differentiate the Li⁺ in the SEI from metallic Li and concluded that unreacted metallic Li, not the (electro)chemically formed Li⁺, dominates the inactive lithium and capacity loss in LMBs.¹⁴ They found that cells with different electrolytes show a similar amount of SEI Li⁺, but a very different amount of unreacted metallic Li. These *ex-situ* techniques help to understand the effect of electrolytes on Li plating in LMBs in different aspects, but fail to capture the kinetics and evolution of Li plating on a temporal scale. Thus, more *in-situ* and operando techniques need to be applied to help understand the relationship between advanced electrolytes and the cycling stability of anode-free LMBs.

In this work, we combine *in-situ* synchrotron X-ray techniques and *ex-situ* lab tools to compare the effect of electrolytes on Li plating distribution and kinetics in anode-free LMBs with a Cu current collector. Three commercially available electrolytes were investigated: traditional carbonate-based electrolyte (LP57), dual-salt electrolyte, and LHCE. The lateral distribution of crystalline Li over the electrode area in anode-free pouch cells was quantified with X-ray diffraction (XRD) mapping. The total non-crystalline Li (amorphous Li and SEI) was derived based on the difference between the electrochemical capacity and diffraction-derived crystalline lithium phase quantification. The degradation mechanisms of anode-free LMBs were uncovered by comparing the lithium of the cells at different stages of cycle life, which explains the different electrochemical performances of cells with these electrolytes. Additionally, operando XRD experiments were designed to investigate the evolution of the amount of the crystalline Li on Cu anode during the Li plating process with different electrolytes. Operando optical cells were further applied to observe the Li plating and stripping process in different electrolytes, which explains different Li morphologies on Cu anode. This study provides insight into the effect of electrolytes on the performance of LMBs, which will in turn help develop anode-free LMBs with high efficiency.

Experimental

Cell fabrication and testing

LiNi_{0.95}Mn_{0.015}Co_{0.02}Al_{0.01}Mg_{0.005}O₂ (NMCAM) and LiNi_{1/3}Mn_{1/3}Co_{1/3}O₂ (NMC111) were used as cathode materials. The hydroxide precursors of the NMCAM and NMC111 powder were obtained with a co-precipitation process.¹⁵ These precursors were mixed with LiOH·H₂O at a molar ratio of 1:1.01 and 1:1.03, followed by a heat treatment at 690°C and 950°C for 15 h, respectively, for NMCAM and NMC111. The active material, conductive carbon black (Super P), and the polyvinylidene fluoride binder with the weight ratio of 90:5:5 were mixed in N-methyl-2-pyrrolidone. The resulting slurry was cast onto an Al foil with a loading of ~ 8 mg cm⁻² for the active material. The obtained cathode electrode was paired with Cu foil to assemble the anode-free cells.

Three types of electrolytes were investigated and compared, including the LP57 electrolyte, the dual-salt electrolyte, and the LHCE. The composition of the LP57 electrolyte is 1 M lithium hexafluorophosphate (LiPF₆) in a mixture of ethylene carbonate and ethyl methyl carbonate (3 : 7 by weight). A 2 wt. % vinylene carbonate additive was added to the LP57 electrolyte. The composition of the dual-salt electrolyte is 0.6 M lithium difluoro(oxalate)borate (LiDFOB) and 0.6 M lithium tetrafluoroborate (LiBF₄) in fluoroethylene carbonate and diethyl carbonate with a ratio of 1 : 2 (by volume). The composition of the LHCE is a mixture of lithium bis(fluorosulfonyl)imide (LiFSI), 1,2-dimethoxyethane, and 1,1,2,2-Tetrafluoroethyl-2,2,3,3-tetrafluoropropyl ether with a molar ratio of 1 : 1.2 : 3. The performance of these three electrolytes was evaluated in CR2032-type coin cells, including anode-free cells with NMCAM as the cathode and Cu foil as the anode, Li|Cu cells, and Li|Li symmetric cells. The anode-free cells were cycled at C/10 rate (1C = 180 mA g⁻¹) for 3 times between 3.5 and 4.4 V, followed by a cycling test with a C/5 charge rate and a C/3 discharge rate for 100 times. The Li|Cu cells were tested at 0.5 mA cm⁻² and 1 mA h cm⁻² to evaluate the Coulombic efficiencies of different electrolytes. The Li|Li symmetric cells were cycled at 1 mA cm⁻² and 2 mA h cm⁻².

Synchrotron X-ray diffraction

Synchrotron XRD measurements were conducted on single-layer pouch cells and CR2016-type window coin cells. The pouch cells were used to study the lateral distribution of crystalline Li on the Cu anode in anode-free cells, while the window coin cells were designed for operando XRD measurements to investigate the kinetics of Li growth.

Anode-free pouch cells were assembled in the lab and shipped to Argonne National Laboratory for XRD characterization at the Advanced Photon Source (APS), beamline 11-ID-B. Nine cells were characterized with the three electrolytes at three different cycling states: first charge (C/5, 4.4 V), first discharge (C/5, 3.5 V), and 30th discharge (C/5, 3.5 V). The X-ray beam spot size was 0.5 mm × 0.5 mm. The XRD mapping was conducted with 1 mm vertical and horizontal step size.

Window coin cells were developed and assembled based on the procedure outlined in our previous studies.^{16,17} The schematic of the window coin cell is shown in Fig. S1 (ESI[†]). Al foil and Cu foil were used to seal the windows (3 mm in diameter) with good long-term stability. To reduce convolution between the Li (110) peak and the NMC (101) peak, NMC111 was selected as the cathode material for the operando study (ESI[†], Fig. S2). A constant current was applied to plate Li on the surface of the Cu anode while continuously collecting XRD data by moving from cell to cell. Two Li plating current densities were investigated: 0.5 mA cm⁻² and 1 mA cm⁻².

Materials characterization

Laboratory materials characterization tools were applied to provide a full picture of Li plating and stripping process. Lab X-ray was utilized to characterize NMC111, LiNi_{0.5}Co_{0.2}Mn_{0.3}O₂, and NMCAM powder from 10° to 80° with a 0.02° scan step (Rigaku Miniflex 600, Cu K α radiation). The XRD patterns were compared to select the best cathode material for the operando XRD study. Scanning electron microscope (SEM, FEI Quanta 650) images were collected to compare the morphologies of Li on the surface of the Cu anode at different points in time. Cells at different states were disassembled inside an Ar-filled glovebox to harvest Cu foils to characterize the Li morphology, including (i) first charge (C/5, 4.4 V), (ii) first discharge (C/5, 3.5 V), and (iii) 100th discharge (3.5 V). Additionally, Li|Cu cells were fabricated to study the evolution of the Li morphology on the Cu anode with the three electrolytes. Li was plated on the Cu anode at a current density of 1 mA cm⁻² for 5 min, 10 min, and 15 min. The Cu foils were harvested, and the Li morphologies were characterized with SEM.

Results and Discussion

Electrochemical performance

The two advanced electrolytes, the dual-salt electrolyte and the LHCE, were found to significantly improve the electrochemical performance of cells compared to the conventional, carbonate-based LP57 electrolyte. Fig. 1(a-c) displays the charge and discharge curves of anode-free cells (NMCAM|Cu) with the three electrolytes in the first three cycles tested between 3.5 and 4.4 V at the C/10 rate. The two advanced electrolytes reduce the overpotential (the voltage difference between the charge curve and the discharge curve) and improve the Coulombic efficiency (CE) of the cells. The CE is only 72.6% in the first cycle for the LP57 electrolyte. By comparison, the dual-salt electrolyte and the LHCE increase the CE to, respectively, 81.1% and 79.6% in the first cycle. Moreover, the CE remains low in the following two cycles for cells with the LP57 electrolyte (around 90%), while it increases to 100% or higher in the cells with the two advanced electrolytes. The 100% CE suggests that all of the plated Li on the Cu anode can be reversibly stripped during cycling.

The CE of an anode-free cell can be related to the morphology of the plated Li. Fig. S3 (ESI[†]) compares the microstructures of Li plated on the Cu anode with different electrolytes. The LP57 electrolyte shows a dendrite-like morphology (Fig. S3a). By comparison, the dual-salt electrolyte shows a sheet-like morphology (Fig. S3b) and

the LHCE shows a noodle-like morphology (Fig. S3c). The Li deposition morphologies in the advanced electrolytes match with existing literature.^{4,18} Moreover, the Li anode thicknesses were estimated with cross-section SEM images. The theoretical thickness of a fully packed Li with 2 mA h cm⁻² loading is 9.7 μ m (the calculation is shown in ESI[†]). Fig. S3(d-f) suggests that the porosity of the plated Li on the Cu anode is the highest in the LP57 electrolytes. Fig. S3(g-l) suggests that the plated Li on the Cu anode is more reversible for the two advanced electrolytes than for the conventional LP57 electrolyte. A large amount of Li stays on the Cu foil with the LP57 electrolyte after discharging. The thickness of the leftover Li is around 5 μ m with an extremely nonuniform distribution (Fig. S3(g and j)). By comparison, the thickness of the leftover Li is only around 2 μ m on the Cu foil with the two advanced electrolytes.

The improved CE leads to better cycling stability of anode-free cells with the two advanced electrolytes compared to the reference LP57 electrolyte. Fig. 1d shows that the cell with the LP57 electrolyte loses all of its capacity within 20 cycles. By comparison, the dual-salt electrolyte extends the cycle number to 100 cycles while the LHCE still maintains around 50% of the initial capacity after 100 cycles. Such a disparity of cycling performance among these cells with different electrolytes can be correlated to the morphology of Li formed on the Cu foil during plating/stripping. For example, the thicknesses derived from the cross-section SEM images in Fig. S3(d-f) indicate that the dual-salt electrolyte and the LHCE reduce the porosity of the plated Li from 53.8% to 39.4% and 30.7% after the first charge. By forming a densely packed Li loading on the Cu anode, the two advanced electrolytes reduced the Li surface area exposed to the electrolytes and thus reduced the side reactions between the Li and the electrolytes. Moreover, Li is more likely to be isolated from the bulk structure in a porous structure during the plating and stripping cycle, forming dead Li incapable of contributing to the cell capacity. Fig. S3(m-o) shows the morphologies of Li on the Cu foils after 100 cycles. A porous dendrite-like or ribbon-like morphology for the LP57 electrolyte is evident. By comparison, the Li had a densely packed sheet-like morphology in the dual-salt electrolyte. Interestingly, the Li in the LHCE showed a starfish-like morphology after 100 cycles.

The electrochemical performance of the three electrolytes was further evaluated in Cu|Li cells and Li|Li symmetric cells, as shown in Fig. 1(e and f). Fig. 1e suggests that the dual-salt electrolyte and to a greater extent the LHCE significantly increased the CE of the Cu|Li cells. The CE of the cell with the LP57 electrolyte falls below 60% within 20 cycles, indicating exponentially worsening performance. The CE of the cell with the dual-salt electrolyte gradually reduces from 98% to 95% after 100 cycles and becomes unstable after 120 cycles. The dual salt electrolyte is known to deplete LiDFOB and LiBF₄ during cycling, and the fluctuating CE after 120 cycles indicates that the salts are irreversibly consumed in the electrolytes.⁴ The CE of the cell with the LHCE is stable during cycling, maintaining 99.3% CE over 300 cycles. Fig. S4 (ESI[†]) displays the plating and stripping curves of the Li|Cu cells and the evolution of the overpotential during cycling. The overpotential of the cell with the LP57 electrolyte increases quickly in the first 20 cycles. The cell with the dual-salt initially has the smallest overpotential, but the overpotential increases exponentially, overtaking the overpotential of the LHCE after 40

cycles. The cell with the LHCE has a relatively stable, gradually rising overpotential during the cycling test. The evolution of the overpotential within the three cells (Fig. S4b, ESI[†]) matches well with the change in the CE shown in Fig. 1e.

Fig. 1f compares the performance of the three electrolytes in Li|Li symmetric cells. The cell with the LHCE shows the best performance with stable voltages during the cycling test. By contrast, cells with the LP57 electrolyte and the dual-salt electrolyte show an unstable voltage after, respectively, 50 h and 200 h of the cycling test. Moreover, the performances of the three electrolytes are

compared further in LMBs with lithium metal as the anode and NMCAM as the cathode. Fig. S5 (ESI[†]) shows that cells with the two advanced electrolytes show better cycling stability than the cell with the LP57 electrolyte. The fast capacity degradation after 100 cycles in the cell with the dual-salt electrolyte results from the consumption of the LiDFOB salt.⁴ Overall, the electrochemical data in Fig. 1 suggest that the LHCE is the best long-term performing electrolyte for anode-free cells among the three electrolytes.

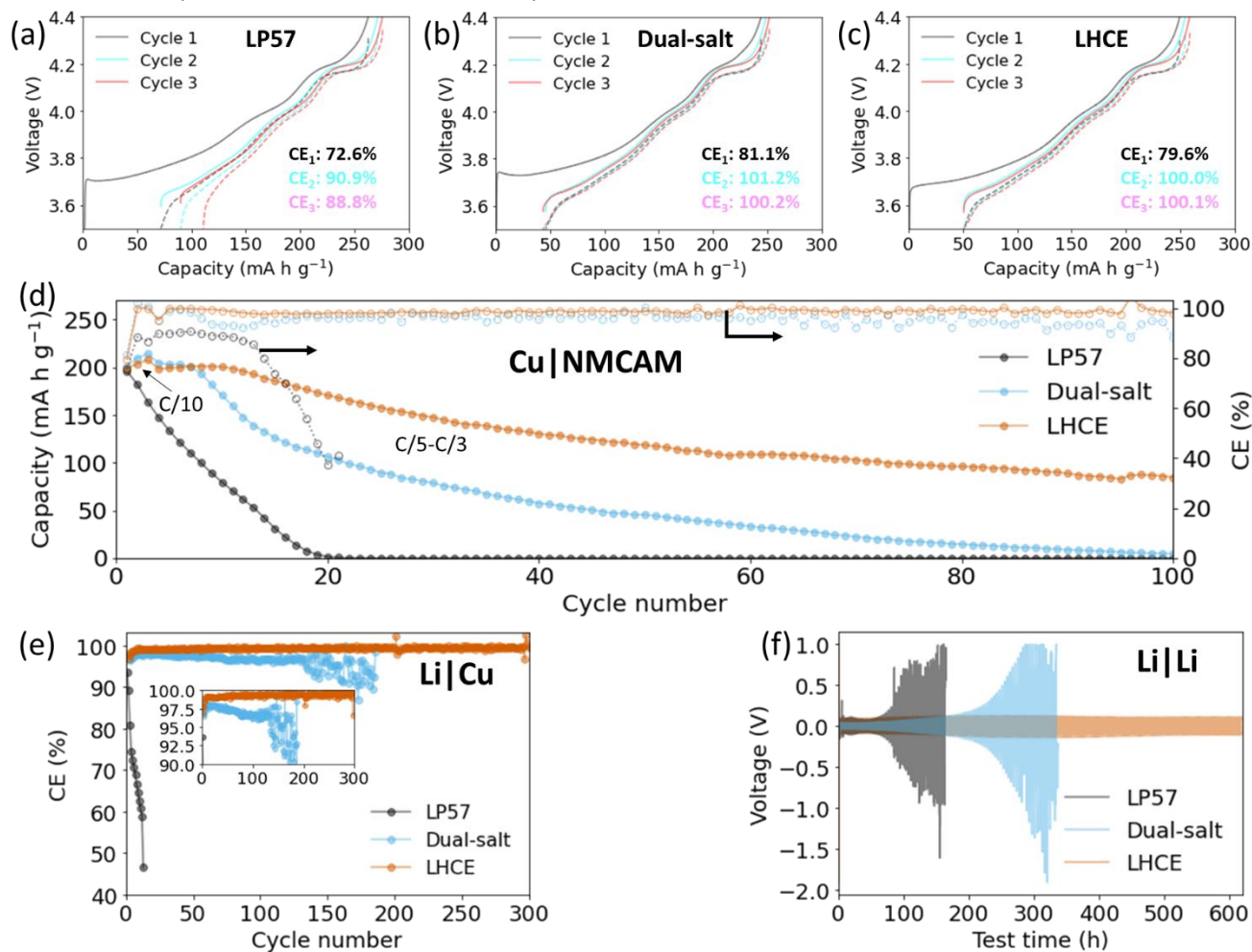


Fig. 1 Electrochemical performance of the cells with three different electrolytes. (a-c) First three cycling curves of NMCAM|Cu anode-free cells with (a) the LP57 electrolyte, (b) the dual-salt electrolyte, and (c) the LHCE tested at C/10 within the voltage range of 3.5 – 4.4 V. The Coulombic efficiencies are listed in each plot. (d) Cycling stability of anode-free cells with the three electrolytes tested at C/5 (charge) and C/3 (discharge). (e) Li metal plating/stripping CEs of the three electrolytes tested in Li|Cu coin cells at 0.5 mA cm⁻² and 1 mA h cm⁻². The insert zooms into a region of the figure for a comparison of the dual-salt and LHCEs. (f) Cycling stability of the three electrolytes evaluated in Li|Li symmetric cells at 1 mA cm⁻² and 2 mA h cm⁻².

Spatial maps of Li distribution in anode-free cells

Efficient, homogeneous Li plating and stripping on the Cu anode is required to achieve high electrochemical performance in anode-free cells. A method to investigate the lateral Li distribution and its evolution on the Cu anode during cycling is needed. Owing to the lack of effective diagnostic tools, investigating the amount and the distribution of Li plated on Cu anode in an anode-free cell is challenging.¹⁴ Postmortem techniques, such as optical microscopy, transmission electron microscopy (TEM), and nuclear magnetic resonance, provide limited information on the plated Li and also require destroying the cell and potentially changing the lithium

conditions due to exposure to gases. Synchrotron-based techniques have been demonstrated to be powerful for operando battery studies.^{19,20} Recently, Charalambous *et al.* demonstrated the effectiveness of synchrotron-based X-ray diffraction (XRD) to detect lateral heterogeneities in lithium intercalation²¹ and the evolution of lithium plating on graphite under fast charging conditions for a single cell over extended cycle life.²² Here, we perform a synchrotron-based lateral XRD mapping technique to measure plated Li on the Cu anode in anode-free cells with a similar procedure. Synchrotron X-ray radiation was used to provide sufficiently high flux to detect Li as it has a low scattering intensity.

Fig. 2 shows a series of two-dimensional maps of the Li distribution at different states for all three electrolytes: in the charged state of the first cycle, the discharged state of the first cycle, and the discharged state after 30 cycles. A total of nine pouch cells were prepared for the mapping study. The ESI⁺ (Fig. S6a) displays the electrochemical data of the first cycle (charged and discharged), while Fig. S6b shows the capacity fade of cells during 30 cycles. The experimental setup for measurement is shown in Fig. S7 (ESI⁺) with an example of the XRD patterns. The Li (110) peak can be identified at a 2θ diffraction angle of 4.88° (Fig. S7c, ESI⁺). As the pouch cell is not rigid, the sample to detector distance varies with the curvature of the cell, resulting in variations to the sample-to-detector distance during the measurement. The current collector, Cu (022) peak was used to re-calibrate the distance for each diffraction pattern to the reference value of 9.492° . The cathode NMC (003) peak (at $\sim 2.5^\circ$) and NMC (113) peak (at $\sim 8.8^\circ$) were used to calculate the lattice parameters (a and c) and the unit cell volume, which is inversely proportional to the amount of Li in the NMCAM cathode.

From an individual XRD pattern, the amount of crystalline Li unit cells as a proportion of the amount of $\text{LiNi}_x\text{Co}_y\text{Mn}_z\text{O}_2$ unit cells can be calculated with the equation (1):

$$\frac{(Li)}{(NMC)} = \left(\frac{I_i^{hkl}}{I_{NMC}^{hkl}} \right) \left(\frac{V_{Li}^2}{V_{NMC}^2} \right) \left(\frac{LPF_{NMC}^{hkl}}{LPF_{Li}^{hkl}} \right) \left(\frac{m_{NMC}^{hkl}}{m_{Li}^{hkl}} \right) \left(\frac{F_{NMC}^{hkl}}{F_{Li}^{hkl}} \right)^2 \quad (1)$$

where I_i^{hkl} is the measured reflection integrated intensity of species i corresponding to a diffraction peak with Miller indices (hkl), V_i is the unit cell volume of species i , LPF_i^{hkl} is the angle-dependent Lorentz-polarization factor that is calculated from formula (2), m_i^{hkl} is the reflection multiplicity, and F_i^{hkl} is the structure factor,

$$LPF_i^{hkl} = \frac{1 + (\cos 2\theta_i^{hkl})^2}{(\sin \theta_i^{hkl})^2 \cos \theta_i^{hkl}} \quad (2)$$

where θ_i is the Bragg angle of species i associated with the specified reflection.

The (110) peak at 4.88° is used for Li, the (003) and (113) peaks at $\sim 2.56^\circ$ and $\sim 8.82^\circ$ are used for NMCAM. It should be noted that the intensities of NMCAM peaks change during charging and discharging, necessitating a correction to the integrated intensity to the number of unit cells. An empirically derived calibration curve is needed to correlate the change in peak intensity to the peak shifts due to delithiation-induced lattice strain. Fig. S8 (ESI⁺) shows an operando XRD measurement of an NMCAM|Li half-cell, from which the calibration curve is derived with the unit cell volume and the (003) integrated intensity can be obtained (Fig. S8f).

As there are two Li atoms in the body-centered cubic lithium unit cell and three Li atoms in the layered-hexagonal $\text{LiNi}_x\text{Co}_y\text{Mn}_z\text{O}_2$ unit cell, the amount of crystalline Li on the Cu foil as a proportion of the original Li sourced from the cathode was calculated from equation (3):

$$\frac{Li_{Li}}{Li_{NMCAM}} = \left(\frac{2}{3} \right) \cdot \frac{(Li)}{(NMC)} \quad (3)$$

where Li_{Li}/Li_{NMCAM} represents the proportion of crystalline Li atoms to original-stoichiometry Li ions in the NMCAM lattice at the detection spot as all Li atoms are from the cathode material.

Fig. 2 (a, d, and g) shows the distribution of plated lithium for all three electrolytes at the charged state of the first cycle. A statistical comparison of the distribution of lithiation states among the three cells is displayed in Fig. 2j. Area averaging indicates that the crystalline Li metal as a proportion of the original cathode lithium is 60.10%, 60.56%, and 64.03%, respectively, with the LP57 electrolyte, dual-salt electrolyte, and LHCE. The charge capacities of the three types of cells are 204 mA h g^{-1} (LP57), 226 mA h g^{-1} (dual-salt), and

241 mA h g^{-1} (LHCE). These capacities correspond to 74.45% (LP57), 82.48% (dual-salt), and 87.96% (LHCE) of the total available Li in the NMCAM cathode, assuming its theoretical capacity is 274 mA h g^{-1} . The mismatch between the charge capacity and the amount of crystalline Li suggests one or more other destinations for the Li: (i) side reactions between Li and residual CuO on the surface of the Cu foil, (ii) consumption of Li as a component in the generation of amorphous solid-electrolyte-interphase (SEI), and (iii) formation of amorphous Li that could not be detected by diffraction methods. These components are assigned as "others" in Fig. 2m. Wang *et al.* claimed that advanced electrolytes promote the formation of amorphous Li based on the postmortem cryo-TEM measurement of around 100 separated random Li ribbons.¹³ The result shown in Fig. 2m agrees with Wang's claim, although the portion of the amorphous Li to the crystalline Li is different in the two studies, which could be from different techniques used for the quantitative analysis. The XRD mapping technique is *in-situ* without the need to disassemble cells to harvest electrodes for the measurement. Moreover, the mapping technique investigates the whole electrode to obtain the statistical result. Thus, the statistical results in Fig. 2m are more accurate than the result obtained from other postmortem techniques.

Fig. 2(b, e, and h) displays the distribution of lithium at the discharged state of the three types of anode-free cells for the first cycle. The cut-off voltage is set to 3.5 V rather than 2.8 V resulting in some reversible Li remaining on the Cu anode. Fig. 2k shows that around 10% - 12% of crystalline Li is left on the Cu anode in all three cells. According to the electrochemical performance shown in Fig. S6, the total leftover Li for all types on the Cu foil is 59 m Ah g^{-1} (LP57), 65 mA h g^{-1} (dual-salt), and 62 mA h g^{-1} (LHCE). These capacities correspond to 21.5% (LP57), 23.8% (dual-salt), and 22.7% (LHCE) of the total available Li. The differences between the total leftover Li and the crystalline Li on the Cu foils are labeled "others" in Fig. 2m. Compared with the charged and discharged samples in the first cycle, it appears that a portion of the "others" is reversible in all three types of cells. These reversible parts may be amorphous Li that is undetectable by XRD but is electrochemically reversible. The cell with the dual-salt electrolyte shows the largest reversible "others" lithium followed by the cell with the LHCE, while the cell with the LP57 electrolyte has the lowest reversible "others" lithium.

Pouch cells with each of the three electrolytes were cycled around 30 times in the lab and then shipped to APS for further XRD mapping studies. The cycling performance of the cells is shown in Fig. S6b with all cells cycled at C/10 rate for the first seven cycles and then cycled at C/5 rate to meet the timeline of the scheduled beamtime at the APS. The cell with the LHCE shows the best long-term cycling performance, while the cell with the LP57 shows the worst performance. Fig. 2(c, f, and i) shows the distribution of crystalline Li on the Cu anode in the three aged cells. Compared to the discharged state of the first cycle (Fig. 2(b, e, and h)), much more crystalline Li is detected after 30 cycles, especially for the cells with the LP57 electrolyte and the dual-salt electrolyte. Additionally, the distribution of the crystalline Li is not uniform in the cell with the LP57 and the dual-salt electrolyte. A bimodal distribution of $\sim 50\%$ and $\sim 75\%$ lithiation for the LP57 and $\sim 30\%$ and $\sim 50\%$ lithiation for the dual-salt electrolyte is evident according to Fig. 2l. By contrast, the LHCE cell had a peak at $\sim 15\%$ lithiation with a sloping tail at higher lithiation, indicating that most of the cell area is still functioning well. The cell with the LP57 has 57.0% crystalline Li out of the total theoretical amount of available Li, while the cell with the LHCE has only 20.2%. The cumulative capacity losses of the three cells are calculated for the first 30 cycles, and the difference between

the cumulative capacity losses and the amount of the crystalline Li indicates that the amount of non-crystalline Li in the anode increases significantly over the long term for the LP57 electrolyte (from 9.5% to 37.9%). By contrast, this non-crystalline Li barely increases for the dual-salt electrolyte (from 13.3% to 16.8%) and the LHCE (from 11.8% to 14.2%). This suggests that the LP57 electrolyte consumes a

significant amount of lithium in the generation of side reactions, such as SEI, which may also isolate plated lithium and prevent it from stripping, resulting in the observed rapid capacity fade. The reduced side reactions of the advanced electrolytes can be attributed to the smaller surface area as the Li is much more densely packed in cells constructed with these electrolytes.

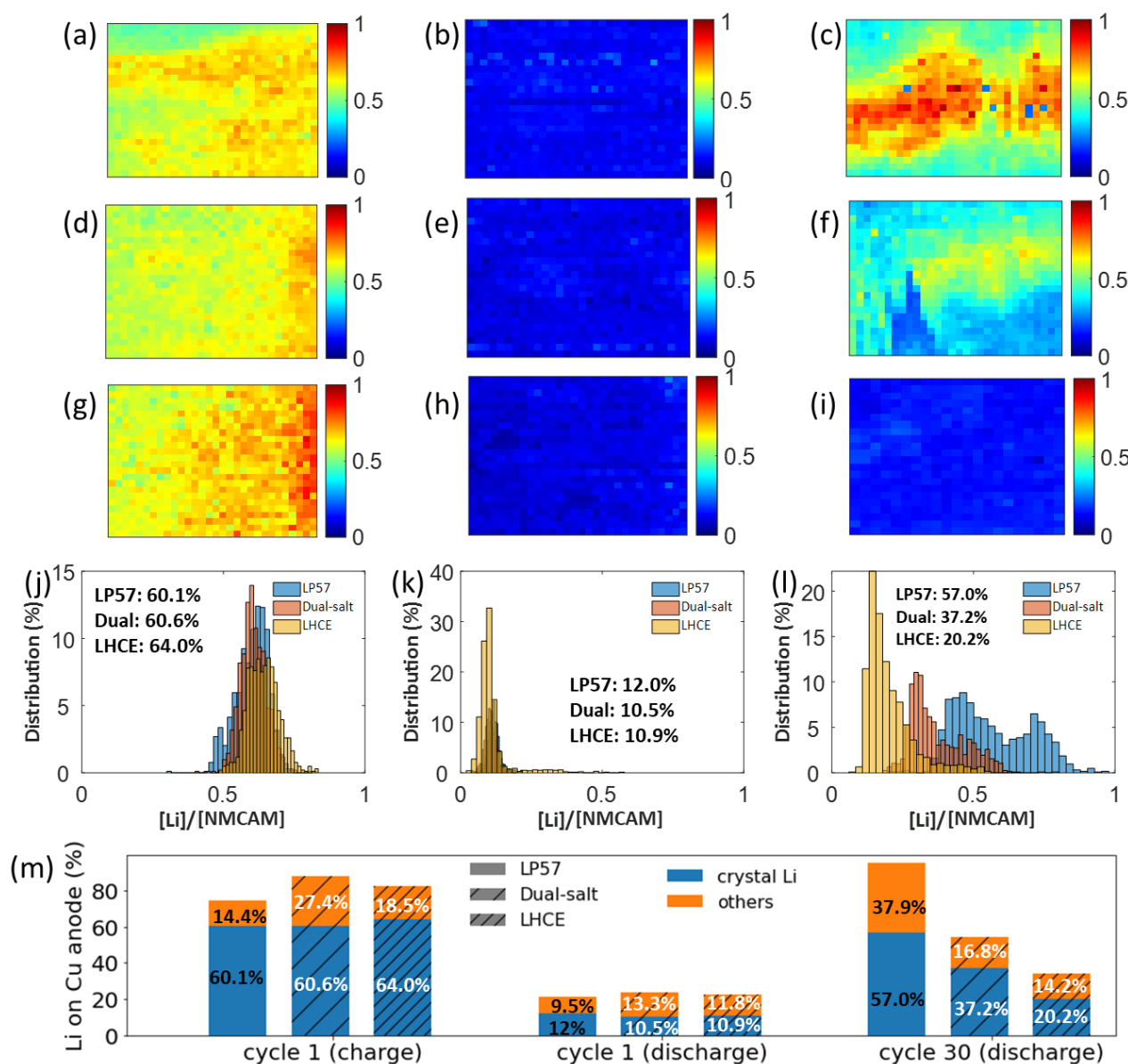


Fig. 2 Spatial synchrotron X-ray diffraction mapping of Li distribution on Cu foil in pouch anode-free cells with (a-c) the LP57 electrolyte, (d-f) dual-salt electrolyte, and (g-i) LHCE. Three different cell states were tested for each electrolyte, including (a, d, g) the charged state of the first cycle, (b, e, h) the discharged state of the first cycle, and (g, h, i) the discharge state after 30 cycles. (j-l) Statistical distribution of crystalline Li on Cu anode at (j) the charged state of the first cycle, (k) the discharged state of the first cycle, and (l) the discharged state after 30 cycles. The mean of the Li amount is listed in each plot. (m) Contribution of crystalline Li and other components on the Cu anode at different states.

Kinetics of Li plating in anode-free cells

To better understand the effect of electrolytes on the kinetics of Li plating and stripping in anode-free cells, operando experiments were conducted to monitor the kinetics of Li plating on Cu current collectors. As previously described, special window coin cells were designed and fabricated for the

operando XRD measurements. The efficacy of the window coin cell has been demonstrated in a previous publication.¹⁶ NMC111 was chosen as the cathode material to reduce the convolution between the Li (110) peak and the NMC (101) peak for the operando study (ESI[†], Fig. S2).

Fig. 3 shows the waterfall plot evolution of XRD intensity during Li plating with a current density of 1 mA cm^{-2} . As the Li (110) peak is located at 4.88° for synchrotron X-ray energy of 58.6 keV, the region of the 2θ value from 4.85° to 4.90° is selected to show the evolution of Li on the Cu anode during the plating process. The unit cell volume of the NMC cathode is used to represent the amount of Li plated on the Cu anode as it monotonically decreased during the de-lithiation process.

The two advanced electrolytes inhibit the formation of crystalline Li. Fig. 3a suggests that crystalline Li appears in the early stage of Li plating with the LP57 electrolyte and that its intensity quickly increases. By comparison, Fig. 3b shows that the crystalline Li signal is relatively low during the Li plating process in the cell with the dual-salt electrolyte and even lower for the LHCE (Fig. 3c). As the same amount of Li moves to the Cu foil based on the electrochemistry, less crystalline Li detected suggests more non-crystalline Li components and/or amorphous Li in the cells with the dual-salt and the LHCEs. To quantitatively compare the amount of crystalline Li formed in the three types of anode-free cells, the Li (110) peak was fitted, and its integrated intensity was normalized to the NMC (003) peak integrated intensity. Fig. 3d compares the evolution of the intensity ratios for all three electrolytes. The results indicate that the crystalline Li forms the earliest and its intensity is the highest in the cell with the LP57 electrolyte. In contrast, the intensity of crystalline Li is the lowest in the cell with the LHCE.

It has been reported that the current density affects the crystallinity of Li during plating, and a small current promotes the formation of amorphous Li.¹³ A current of 0.5 mA cm^{-2} was also applied for Li plating during the operando XRD experiment. Fig. S9 (ESI[†]) suggests that less crystalline Li is formed with the LP57 electrolyte at 0.5 mA cm^{-2} compared to the Li plating at 1 mA cm^{-2} (Fig. 3d). In addition, a similar relationship among the three electrolytes is found when the plating current is reduced from 1 mA cm^{-2} to 0.5 mA cm^{-2} , where the cell with the LP57 electrolyte has the most crystalline Li while the cell with the LHCE electrolyte has the least.

Table S1 (ESI[†]) summarizes the crystallinity of electrochemically deposited Li in different electrolytes in recent studies. The preferred growth direction of crystalline Li depends on the plating current density, the plating capacity, and electrolytes.^{23–25} Although crystalline Li is always observed, amorphous Li has only been observed in very few studies.^{13,26} Wang et al. found that the small current density and ether-based LHCE promote the formation of amorphous Li during Li plating.¹³ In addition, they carried out reactive molecular dynamics simulation to understand the formation of amorphous Li, which depends on current density and deposition time. However, the interactions between electrolytes and Li nucleation and growth were not investigated, which warrants further investigation to guide electrolyte design.

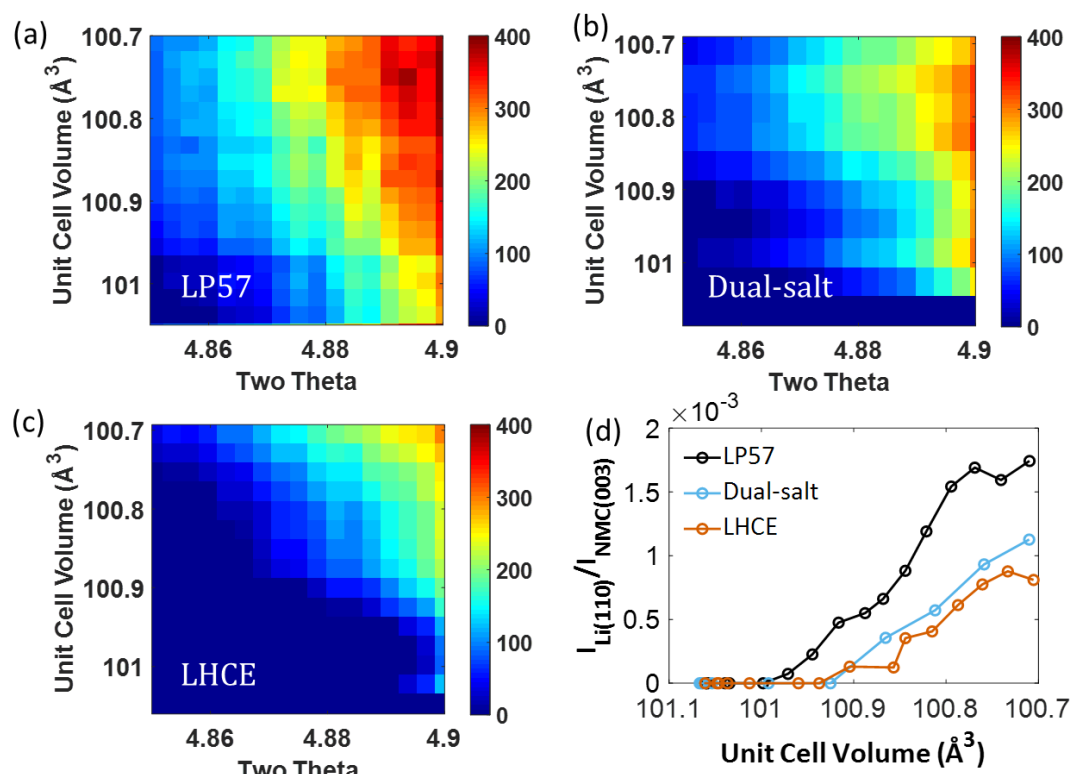


Fig. 3 Operando XRD measurement of the growth of Li on Cu anode with three different electrolytes, including (a) the LP57 electrolyte, (b) the dual-salt electrolyte, and (c) the LHCE. The cathode is NMC111 and the anode is Cu foil. The Li plating current was 1 mA cm^{-2} . The NMC unit cell volume is used as the y-axis in the three contour plots (a-c) because it monotonically decreases with the amount of Li plating on the Cu anode. (d) Evolution of the Li (110) peak intensity during the plating process for the three types of anode-free cells. The Li intensity is normalized by the intensity of the NMC (003) to account for the synchrotron beam fluctuation during the measurement.

To uncover the evolution of the plated Li morphology with different electrolytes, SEM micrographs were collected after different plating times: 5 min, 10 min, and 15 min. Fig. 4(a-c) shows that the plated Li forms a porous structure with the LP57 electrolyte. At the very beginning (5 min), porous Li is randomly plated on the Cu anode surface with a large pore size ($50\ \mu\text{m}$ - $100\ \mu\text{m}$). It is possible that the plated Li and/or SEI layer induces a modified Li^+ diffusion field, making the region favorable for Li^+ diffusion.¹² For example, Fig. 4b shows that the pore size is reduced to $20\ \mu\text{m}$ - $30\ \mu\text{m}$ after 10 min of plating. The pore size is further reduced to below $10\ \mu\text{m}$ after 15 min of plating (Fig. 4c). These results suggest that Li grows within the existing large pores, which gradually makes the pore sizes smaller and smaller during the plating process. Moreover, Fig. S10 suggests that a large percentage of the Cu foil is bare of Li even after 15 min of plating. Therefore, the plated Li is both porous and highly inhomogeneous for the cell with the LP57 electrolyte.

By contrast, the dual-salt electrolyte and the LHCE help form a well-packed Li layer on the Cu foil. Fig. 4(d-f) shows the Li

morphologies with the dual-salt electrolyte after 5 min, 10 min, and 15 min. The Cu foil is fully covered with Li with no remaining bare Cu even with the 5 min plating, suggesting a uniform growth of Li over the surface of the Cu foil. There are cracks on the surface of the Li, which may indicate the interface of Li grown from multiple nucleation sites on the Cu foil. These cracks may become the new nucleation sites for further Li growth, gradually reducing the distance between cracks during the plating process, as shown in Fig. 4(e and f). Fig. 4(g-i) and Fig. S11 (ESI[†]) suggest that Li shows noodle-like morphology with the LHCE. The diameter of the "noodle" is around $1\ \mu\text{m}$, and it does not change significantly during the plating process. More importantly, the growth direction of the "noodle" is in parallel with the surface of the Cu foil. Such a growth direction is proposed to be beneficial for the formation of a well-packed Li morphology on the Cu foil (ESI[†], Fig. S3(c and f)).

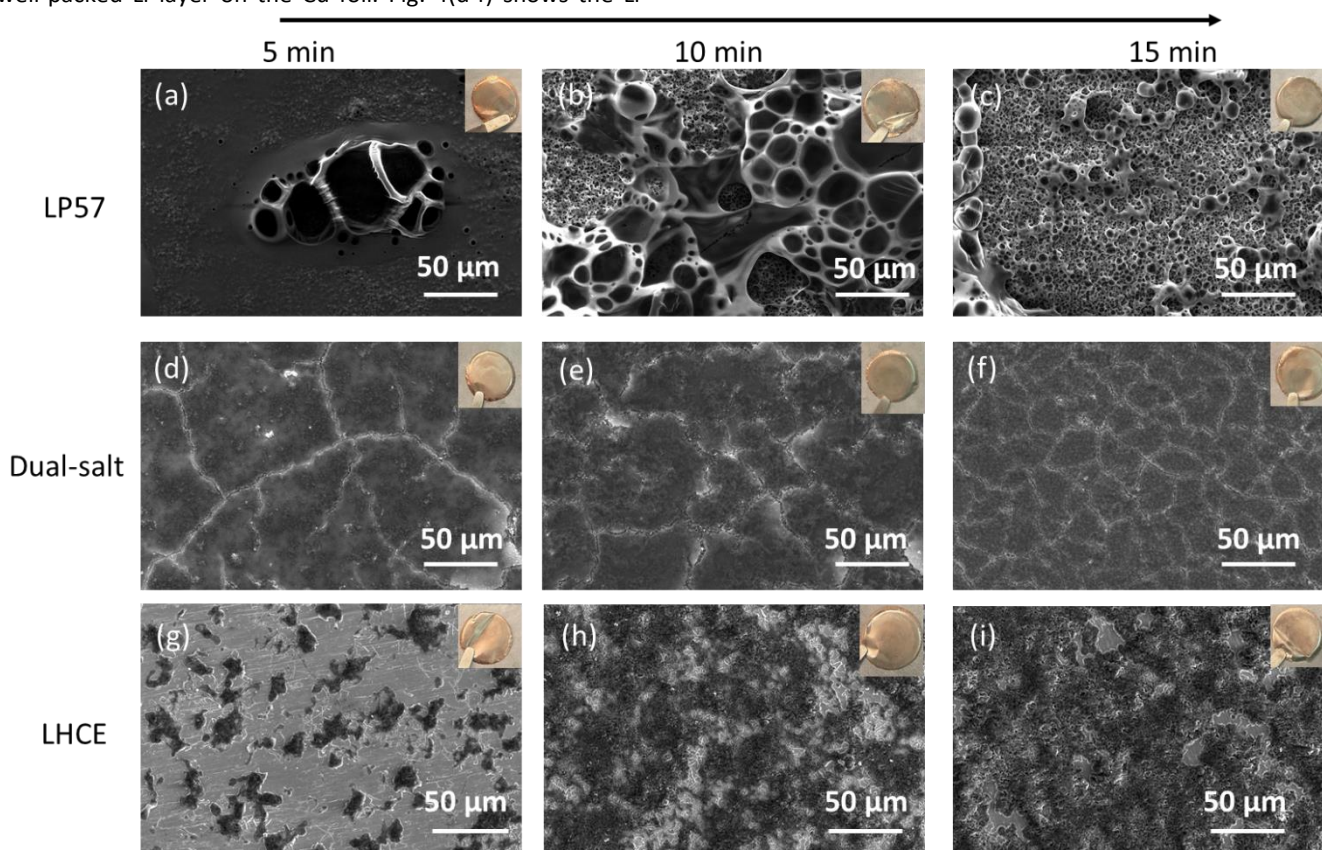


Fig. 4. Evolution of Li morphology on the Cu anode in (a-c) the LP57 electrolyte, (d-e) dual-salt electrolyte, and (g-i) LHCE. Li is plated for (a, d, g) 5 min, (b, e, h) 10 min, and (c, f, i) 15 min with the current density of $1\ \text{mA cm}^{-2}$. The inset is a picture of the Cu anode current collector that is disassembled from coin cells. The scale bar is inserted in each plot.

An optical Li|Li symmetric cell was utilized to visualize the growing process of Li in the perpendicular direction to a Li disc. (ESI[†], Fig. S12). Fig. S13 compares the Li plating process in the three

electrolytes at the current density of $1\ \text{mA cm}^{-2}$ and the capacity of $2\ \text{mA h cm}^{-2}$. The details of the Li plating and stripping process are further presented in the supporting videos (SI video1_optical cell

(LP57).mp4, SI video2_optical cell (Dual_salt).mp4, SI video3_optical cell (LHCE).mp4).

The morphology of plated Li and its growth process is fundamentally different in the LP57 electrolyte compared to the two advanced electrolytes. Evidence presented in Fig. S13a and SI video1 suggests that plated Li nucleates at only a few active sites on the surface of the Li electrode at the beginning for LP57. The plated Li at these spots attracts Li-ions and continues to a growth phase, leading to an extremely heterogeneous morphology. This growth behavior matches the snapshots presented in the SEM images in Fig. 4(a-c), where Li^+ preferentially deposits on the already existing plated Li particles during the plating process. It should be mentioned that the optical view must be adjusted properly to focus on the few plated Li sites to observe the Li growth process due to the extremely heterogeneous Li morphology, which explains why the edges of the Li electrodes in Fig. S13a are out of focus.

SI video2 and SI video3 present, respectively, the Li plating and stripping process in the dual-salt electrolyte and the LHCE. A few snapshots of the Li plating process are also shown in Fig. S13b and Fig. S13c. In both advanced electrolytes, Li nucleates and grows over the entire surface of the Li electrode, leading to uniform Li morphologies. The evolution of the cross-section Li optical images also matches the SEM snapshots in Fig. 4(d-f) and Fig. 4(g-i), where the plated Li have dense and well-packed morphologies for the two advanced electrolytes.

Understanding the role of electrolytes on the dynamics of Li plating and stripping

The experimental results show that advanced electrolytes, including dual-salt electrolyte and LHCE, significantly improve the electrochemical performance of anode-free cells compared to the standard, carbonate-based LP57 electrolyte. Such an improvement is linked to the Li crystallinity and morphology on the Cu foil.

The lithium loss per-cycle is relevant to the total electrolyte/Li electrode interfacial area.^{27,28} Cui's group observed large and homogeneous Li nuclei when suppressing the nucleation over-potential by reducing the plating current²⁷ or increasing the temperature²⁸. The large granular Li reduces the exposed area to the electrolyte and decreases the lithium loss during cycling. Here, we find that different electrolytes lead to different Li components and crystallinities on Cu anode current collector in the beginning stage of Li plating, where amorphous lithium formed by advanced electrolytes are beneficial to form a dense and well-packed Li morphology (Fig. S3). For example, Fig. S3(d-f) suggests that the porosity of the plated Li is reduced from 53.8% (LP57) to 39.4% (dual-salt) and 30.7% (LHCE) after the first charge. The reduced porosity decreases the exposed surface area to the electrolyte, and thus improves cycling stability.

The dense and well-packed Li morphology in the advanced electrolytes could be from the more amorphous Li formed at the beginning of Li plating (Fig. 3). Literature shows that amorphous Li outperforms crystalline Li with respect to electrochemical reversibility by forming grains with higher

density, lower porosity and tortuosity, less reactivity, and better microstructure interconnections.⁴³ The favorable Li morphology is from the amorphous nature that avoids epitaxial growth, promoting multi-dimensional growth into large grains. These large grains not only reduce the side reactions between Li and the electrolyte but also provide better structural electronic connections, which has been proposed as a crucial aspect that leads to the formation of inactive metallic lithium during cycling.¹⁴

The Li plating morphology on the Cu anode is also relevant to the reduction of Li salt and solvents in electrolytes, which is closely related to the energy of their lowest unoccupied molecular orbital (LUMO). Existing literature shows that the reduction potential of the four investigated salts decreases in the order of $\text{LiBF}_4 > \text{LiPF}_6 > \text{LiFSI} > \text{LiDFOB}$, indicating that LiFSI and LiDFOB are easily reduced at the anode-electrolyte interface.^{29,30} The reduction of these salts forms inorganic-rich solid interphase on the surface of the Cu anode. Such solid interphase is beneficial for homogeneous Li deposition. For example, Cao *et al.* observed a uniform and thin SEI with a high fraction of inorganic species formed in an ether-based solvent with LiFSI as the conducting salt.³¹ Jurng *et al.* reported that the electrolyte with the LiDFOB salt (carbonate solvent) generates a uniform film composed of nanostructured LiF particles covered by a smooth layer of Li_2CO_3 and lithium oxalate.³² The interphase layer has homogeneous composition, promoting the uniform Li plating by modifying the Li^+ diffusion field that regulates Li deposition. In addition, Hou *et al.* reported a simultaneous growth of inorganic-organic bilayer solid interphase in conventional carbonate-based electrolyte with 1 M LiPF₆ salt.³² The inorganic-organic heterogeneous composition of the interphase causes inhomogeneity of the Li^+ flux, resulting in uneven Li plating and mechanical failure of the solid interphase. Therefore, a Li salt with a low reduction potential paired with solvents with a relatively high reduction potential can be beneficial to the Li plating process. A small portion of these salts could also be used as additives to improve the performance of LMBs. Such an understanding will help develop advanced electrolytes for developing stable (anode-free) LMBs.

Besides the intrinsic salt and solvents stability, the electrolyte solvation structure^{33,34} and the salt concentration^{35,36} also affect the electrolyte decomposition, and thus the SEI composition and morphology during cycling. For example, in high-concentration electrolyte and LHCE, salt anions enter the solvation sheath, forming contact ion pairs and cation-anion aggregates.³³ Such a unique solvation structure promotes the decomposition of anions and forms an inorganic-rich SEI, such as LiF. The LiF-rich SEI is believed to be thin and dense with enhanced mechanical properties, which could be beneficial to form a dense and well-packed Li morphology during Li plating. In addition, according to Nernst equation, the Li/Li^+ potential at the electrode increases with the salt concentration.³⁵ The increased Li/Li^+ potential would affect the SEI composition and the lithium plating process. Therefore, adjusting the salt concentration and designing the solvation

structure of electrolytes are promising strategies to realize highly reversible Li plating and stripping in anode-free cells.

Wang *et al.* have applied *ex-situ* cryo-TEM to quantify the amount of crystalline Li in different electrolytes.¹³ By analyzing ~ 100 separated random Li ribbons, they found that the deposited Li consists of 52.6% and 47.6% of crystalline Li and amorphous Li, respectively, in the baseline electrolyte. In contrast, the deposited Li in the advanced electrolyte (LHCE) consists of 23.2% and 76.8% of crystalline Li and amorphous Li, respectively. Here, *in-situ* synchrotron XRD mapping was applied to study the amount of crystalline Li on the Cu anode. Although the difference among the electrolytes for the ratio of crystalline Li to the total plated Li (Fig. 2m) was not as large as that in Wang's report, the conclusion is similar in both studies that advanced electrolytes promote the formation of amorphous Li in LMBs. For example, Fig. 2m suggests that the non-crystalline Li components (amorphous Li and SEI) increase by only ~ 3% after 30 cycles for the two advanced electrolytes. By comparison, the irreversible crystalline Li increases 26.7% for the cell with the dual-salt electrolyte and 9.3% for the cell with the LHCE after 30 cycles. These findings also agree well with Fang *et al.*'s study, which shows that electrochemically isolated metallic Li rather than the (electro)chemically formed Li⁺ in the SEI dominates the inactive lithium and capacity loss.¹⁴ Thus, developing an advanced electrolyte that can eliminate the dead crystalline lithium during cycling would significantly improve the electrochemical performance of (anode-free) LMBs.

Conclusions

Three commercially available electrolytes were compared for application to anode-free LMBs: conventional LP57 electrolyte, dual-salt electrolyte, and LHCE. The two advanced electrolytes outperform the conventional LP57 electrolyte in the aspects of Coulombic efficiency, cycling stability, and overpotential. The advanced electrolytes help form a dense and well-packed metallic Li on Cu anode current collector during Li plating, leading to a relatively small surface area exposed to the electrolyte, thus fewer unwanted side reactions. Results from the XRD mapping of aged pouch cells show that the capacity fade of anode-free cells is dominated by the irreversible crystalline Li (dead Li) buildup on the Cu anode. Developing an electrolyte that can reduce the formation of electrochemically isolated dead Li during cycling is key to enabling the cycling stability of (anode-free) LMBs.

Multi-modal operando XRD and operando optical imaging provide a guide to the Li plating kinetics for different electrolytes. The two advanced electrolytes appear to promote the formation of non-crystalline Li components in the beginning stages of Li plating, including the SEI layer and amorphous Li. These components are beneficial to Li growth by providing sufficient Li nucleation sites and leading to uniform growth during the plating process. Non-destructive techniques are crucial to studying the kinetics of anode-free LMBs during cycling. However, the complexity of real cells and the weak interaction between X-rays and Li metal necessitates the use of

high-energy and high flux X-rays provided by modern synchrotrons. Synchrotron diffraction is non-destructive and provides quantitative phase information of different components within a cell. The combination of multi-modal operando tools and *ex-situ* techniques provides a detailed understanding of the Li plating and stripping behavior in different electrolytes. Such an understanding will in turn inform strategies for developing better electrolytes and provide a method to analyze the effects of these electrolytes, which will enable high-performance, safe LMBs with long cycle life.

Author Contributions

Laisuo Su: Conceptualization, Methodology, Validation, Investigation, Resources, Writing - original draft, Visualization. **Harry Charalambous:** Methodology, Resources, Validation, Investigation. **Zehao Cui:** Resources, Investigation. **Arumugam Manthiram:** Conceptualization, Writing - review & editing, Supervision, Project administration, Funding acquisition.

Conflicts of interest

The corresponding author (A. M.) is a co-founder of TexPower, Inc., a start-up company focusing on cobalt-free cathode materials for lithium-based batteries.

Acknowledgments

This work was supported by the Assistant Secretary for Energy Efficiency and Renewable Energy, Office of Vehicle Technologies of the U.S. Department of Energy through the Advanced Battery Materials Research (BMR) Program (Battery500 Consortium) award number DE-EE0007762. The research used resources of the Advanced Photon Sources, a U.S. Department of Energy (DOE) office of Science User Facility operated for the DOE Office of Science, Office of Basic Energy Sciences, by Argonne National Laboratory under Contract No. DE-AC02-06CH11357. The authors thank Dr. Jiarui He for assistance with the optical cell experiment, Mr. Jayse Langdon for helpful discussion.

References

- 1 Y. Kim, W. M. Seong and A. Manthiram, *Energy Storage Materials*, 2020.
- 2 A. Manthiram, *NAT COMMUN*, 2020, **11**.
- 3 P. Albertus, S. Babinec, S. Litzelman and A. Newman, *NAT ENERGY*, 2018, **3**, 16-21.
- 4 A. J. Louli, A. Eldesoky, R. Weber, M. Genovese, M. Coon, J. DeGooyer, Z. Deng, R. T. White, J. Lee, T. Rodgers, R. Petibon, S. Hy, S. J. H. Cheng and J. R. Dahn, *NAT ENERGY*, 2020, **5**, 693-702.
- 5 S. Nanda, A. Gupta and A. Manthiram, *ADV ENERGY MATER*, 2021, **11**, 2000804.

- 6 Y. Zhang, W. Luo, C. Wang, Y. Li, C. Chen, J. Song, J. Dai, E. M. Hitz, S. Xu, C. Yang, Y. Wang and L. Hu, *Proceedings of the National Academy of Sciences*, 2017, **114**, 3584-3589.
- 7 Y. Gao, Z. Yan, J. L. Gray, X. He, D. Wang, T. Chen, Q. Huang, Y. C. Li, H. Wang, S. H. Kim, T. E. Mallouk and D. Wang, *NAT MATER*, 2019, **18**, 384-389.
- 8 Z. Yu, H. Wang, X. Kong, W. Huang, Y. Tsao, D. G. Mackanic, K. Wang, X. Wang, W. Huang, S. Choudhury, Y. Zheng, C. V. Amanchukwu, S. T. Hung, Y. Ma, E. G. Lomeli, J. Qin, Y. Cui and Z. Bao, *NAT ENERGY*, 2020, **5**, 526-533.
- 9 F. Ospina-Acevedo, N. Guo and P. B. Balbuena, *J MATER CHEM A*, 2020, **8**, 17036-17055.
- 10 S. Jiao, X. Ren, R. Cao, M. H. Engelhard, Y. Liu, D. Hu, D. Mei, J. Zheng, W. Zhao, Q. Li, N. Liu, B. D. Adams, C. Ma, J. Liu, J. Zhang and W. Xu, *NAT ENERGY*, 2018, **3**, 739-746.
- 11 X. Ren, L. Zou, X. Cao, M. H. Engelhard, W. Liu, S. D. Burton, H. Lee, C. Niu, B. E. Matthews, Z. Zhu, C. Wang, B. W. Arey, J. Xiao, J. Liu, J. Zhang and W. Xu, *Joule*, 2019, **3**, 1662-1676.
- 12 S. Jurng, Z. L. Brown, J. Kim and B. L. Lucht, *ENERG ENVIRON SCI*, 2018, **11**, 2600-2608.
- 13 X. Wang, G. Pawar, Y. Li, X. Ren, M. Zhang, B. Lu, A. Banerjee, P. Liu, E. J. Dufek, J. Zhang, J. Xiao, J. Liu, Y. S. Meng and B. Liaw, *NAT MATER*, 2020, **19**, 1339-1345.
- 14 C. Fang, J. Li, M. Zhang, Y. Zhang, F. Yang, J. Z. Lee, M. Lee, J. Alvarado, M. A. Schroeder, Y. Yang, B. Lu, N. Williams, M. Ceja, L. Yang, M. Cai, J. Gu, K. Xu, X. Wang and Y. S. Meng, *NATURE*, 2019, **572**, 511-515.
- 15 S. Lee, W. Li, A. Dolocan, H. Celio, H. Park, J. H. Warner and A. Manthiram, *ADV ENERGY MATER*, 2021, 2100858.
- 16 L. Su, P. Choi, N. Nakamura, H. Charalambous, S. Litster, J. Ilavsky and B. Reeja-Jayan, *APPL ENERG*, 2021, **299**, 117315.
- 17 L. Su, P. Choi, B. S. Parimalam, S. Litster and B. Reeja-Jayan, *MethodsX*, 2021, **8**, 101562.
- 18 S. Chen, J. Zheng, D. Mei, K. S. Han, M. H. Engelhard, W. Zhao, W. Xu, J. Liu and J. G. Zhang, *ADV MATER*, 2018, **30**, 1706102.
- 19 L. Su, J. L. Weaver, M. Groenenboom, N. Nakamura, E. Rus, P. Anand, S. K. Jha, J. S. Okasinski, J. A. Dura and B. Reeja-Jayan, *ACS APPL MATER INTER*, 2021, **13**, 9919-9931.
- 20 L. Su, S. K. Jha, X. L. Phuah, J. Xu, N. Nakamura, H. Wang, J. S. Okasinski and B. Reeja-Jayan, *J MATER SCI*, 2020, **55**, 12177-12190.
- 21 H. Charalambous, D. P. Abraham, A. R. Dunlop, S. E. Trask, A. N. Jansen, T. R. Tanim, P. R. Chinnam, A. M. Colclasure, W. Xu, A. A. Yakovenko, O. J. Borkiewicz, L. C. Gallington, U. Ruett, K. M. Wiaderek and Y. Ren, *J POWER SOURCES*, 2021, **507**, 230253.
- 22 H. Charalambous, O. J. Borkiewicz, A. M. Colclasure, Z. Yang, A. R. Dunlop, S. E. Trask, A. N. Jansen, I. D. Bloom, U. Ruett, K. M. Wiaderek and Y. Ren, *ACS Energy Letters*, 2021, **6.10**, 3725-3733
- 23 Y. Li, Y. Li, A. Pei, K. Yan, Y. Sun, C. L. Wu, L. M. Joubert, R. Chin, A. L. Koh, Y. Yu, J. Perrino, B. Butz, S. Chu and Y. Cui, *SCIENCE*, 2017, **358**, 506-510.
- 24 Q. Zhao, Y. Deng, N. W. Utomo, J. Zheng, P. Biswal, J. Yin and L. A. Archer, *NAT COMMUN*, 2021, **12**.
- 25 X. Cao, X. Ren, L. Zou, M. H. Engelhard, W. Huang, H. Wang, B. E. Matthews, H. Lee, C. Niu, B. W. Arey, Y. Cui, C. Wang, J. Xiao, J. Liu, W. Xu and J. Zhang, *NAT ENERGY*, 2019, **4**, 796-805.
- 26 X. Wang, M. Zhang, J. Alvarado, S. Wang, M. Sina, B. Lu, J. Bouwer, W. Xu, J. Xiao, J. Zhang, J. Liu and Y. S. Meng, *NANO LETT*, 2017, **17**, 7606-7612.
- 27 A. Pei, G. Zheng, F. Shi, Y. Li and Y. Cui, *NANO LETT*, 2017, **17**, 1132-1139.
- 28 J. Wang, W. Huang, A. Pei, Y. Li, F. Shi, X. Yu and Y. Cui, *NAT ENERGY*, 2019, **4**, 664-670.
- 29 J. Zheng, M. H. Engelhard, D. Mei, S. Jiao, B. J. Polzin, J. Zhang and W. Xu, *NAT ENERGY*, 2017, **2**.
- 30 R. Younesi, G. M. Veith, P. Johansson, K. Edström, T. Vegge and O. R. T. U. Oak Ridge National Lab. ORNL, *ENERG ENVIRON SCI*, 2015, **8**, 195-1922.
- 31 X. Cao, X. Ren, L. Zou, M. H. Engelhard, W. Huang, H. Wang, B. E. Matthews, H. Lee, C. Niu, B. W. Arey, Y. Cui, C. Wang, J. Xiao, J. Liu, W. Xu and J. Zhang, *NAT ENERGY*, 2019, **4**, 796-805.
- 32 C. Hou, J. Han, P. Liu, C. Yang, G. Huang, T. Fujita, A. Hirata and M. Chen, *ADV ENERGY MATER*, 2019, **9**, 1902675.
- 33 J. Zheng, J. A. Lochala, A. Kwok, Z. D. Deng and J. Xiao, *ADV SCI*, 2017, **4**, 1700032
- 34 Y. Yamada and A. Yamada, *J ELECTROCHEM SOC*, 2015, **162**, A2406-A2423.
- 35 K. Ueno, R. Tatara, S. Tsuzuki, S. Saito, H. Doi, K. Yoshida, T. Mandai, M. Matsugami, Y. Umebayashi, K. Dokko and M. Watanabe, *PHYS CHEM CHEM PHYS*, 2015, **17**, 8248-8257.
- 36 H. Moon, T. Mandai, R. Tatara, K. Ueno, A. Yamazaki, K. Yoshida, S. Seki, K. Dokko and M. Watanabe, *The Journal of Physical Chemistry C*, 2015, **119**, 3957-3970.